Amplitude modulation schemes for enhancing acoustically-driven microcentrifugation and micromixing

Kar M. Ang,[1] Leslie Y. Yeo,[2] Yew M. Hung,[1] and Ming K. Tan[1,a)]
[1]*School of Engineering, Monash University Malaysia, 47500 Bandar Sunway, Selangor, Malaysia*
[2]*Micro/Nanophysics Research Laboratory, RMIT University, Melbourne, VIC 3001, Australia*

(Received 2 September 2016; accepted 8 September 2016; published online 20 September 2016)

The ability to drive microcentrifugation for efficient micromixing and particle concentration and separation on a microfluidic platform is critical for a wide range of lab-on-a-chip applications. In this work, we investigate the use of amplitude modulation to enhance the efficiency of the microcentrifugal recirculation flows in surface acoustic wave microfluidic systems, thus concomitantly reducing the power consumption in these devices for a given performance requirement—a crucial step in the development of miniaturized, integrated circuits for true portable functionality. In particular, we show that it is possible to obtain an increase of up to 60% in the acoustic streaming velocity in a microdroplet with kHz order modulation frequencies due to the intensification in Eckart streaming; the streaming velocity is increasing as the modulation index is increased. Additionally, we show that it is possible to exploit this streaming enhancement to effect improvements in the speed of particle concentration by up to 70% and the efficiency of micromixing by 50%, together with a modest decrease in the droplet temperature. *Published by AIP Publishing.* [http://dx.doi.org/10.1063/1.4963103]

I. INTRODUCTION

The ability to drive intense micromixing and rapid particle concentration at the microscale is notoriously difficult due to the laminarity of flow that is typical of conventional microfluidic devices, as reflected by the Reynolds numbers associated with flows in these devices, which are commonly order 1 and below (Stone *et al.*, 2004). Many attempts have been made to address poor mixing in these devices, which include the fabrication of structures and channel geometries to passively disrupt the flow laminarity, or the introduction of external fields, e.g., electric, magnetic, and acoustic fields, among others, to actively drive chaotic advection (Nguyen and Wu, 2005). Passive mixing strategies, while simple, however, often require fabrication of complex geometries, whereas the active mixers often require large and cumbersome benchtop ancillary equipment such as signal generators, amplifiers, and capillary pumps, which prohibit miniaturization and integration of the microfluidic device when true portability is required in some applications (Yeo *et al.*, 2011). Concomitantly, it is even more difficult to drive centrifugal recirculation in microfluidic devices to exploit hydrodynamic concentration of particles for sample preconcentration, which is extremely useful, for example, for purification (e.g., separation of red blood cells from plasma) or as a means to increase detection speed, sensitivity, and selectivity in biosensors (Yeo *et al.*, 2011). Most attempts to achieve particle concentration in microfluidic devices have been to employ trapping forces, generated optically (Dholakia *et al.*, 2008), electrically (Cheng *et al.*, 2007; Cho *et al.*, 2007; Hwang and Park, 2009; Lewpiriyawong *et al.*, 2012; and Harrison *et al.*, 2015), acoustically (Laurell *et al.*, 2007 and

a)Electronic mail: tan.ming.kwang@monash.edu

Lin *et al.*, 2012), or magnetically (Pamme *et al.*, 2006 and Zeng *et al.*, 2013), to drive local aggregation. A disadvantage of these schemes in addition to similar constraints in the necessity for large ancillary equipment for the provision of external fields, however, is that such trapping is only useful under stationary or weakly flowing conditions as the hydrodynamic drag forces arising from the flow in drops and channels are usually sufficient to cause dispersion of the aggregated particle clusters.

Surface acoustic waves (SAWs) offer an attractive alternative to these technologies to induce micromixing and particle concentration, together with the possibility for driving a wide suite of microfluidic operations (Yeo and Friend, 2014; Ding *et al.*, 2013; and Destgeer and Sung, 2015) such as droplet and microchannel transport (Schmid *et al.*, 2012; Baudoin *et al.*, 2012; Dentry *et al.*, 2014; Collingnon *et al.*, 2015; and Jung *et al.*, 2016), particle trapping (Shi *et al.*, 2008, 2009; Chen *et al.*, 2014; Destgeer *et al.*, 2013, 2014, and 2015), cooling and heating (Kondoh *et al.*, 2009; Shilton *et al.*, 2015; and Ang *et al.*, 2015), and jetting and atomization (Qi *et al.*, 2008; Tan *et al.*, 2009; and Winkler *et al.*, 2015). The underlying mechanism that enables these operations is the acoustic streaming (Yeo and Friend, 2014) that arises from the fluid–structural interactions associated with the undulating boundary as the SAW traverses the surface of the piezoelectric substrate beneath the fluid (Manor *et al.*, 2012 and 2015). Not only is SAW acoustic streaming an efficient means for driving chaotic micromixing (Frommelt *et al.*, 2008b; Shilton *et al.*, 2011; and Jo and Guldiken, 2013) but it also has the advantage of battery-powered operation via a portable driver circuit, therefore permitting miniaturization and integration of the entire actuation platform together with the chip-based operation (Martins *et al.*, 2014). More recently, Shilton *et al.* (2014) demonstrated downward scalability to nanolitre volumes while still maintaining the ability to rapidly mix the fluids in a droplet, made possible by increasing the SAW frequency to GHz order (Dentry *et al.*, 2014). On the other hand, the same SAW platform has been shown to be a powerful tool for driving chip-scale microcentrifugation, in which the azimuthal flow recirculation (in a droplet) that arises is sufficiently intense to rapidly concentrate particles suspended in the flow (Shilton *et al.*, 2008; Glass *et al.*, 2012; Li *et al.*, 2007; and Destgeer *et al.*, 2016), which can then be exploited for sample preconcentration to enhance biomolecular detection sensitivity and selectivity (Bourquin *et al.*, 2011).

Parenthetically, we note a similar technique that relies on azimuthal recirculation to induce micromixing and particle concentration has been earlier demonstrated through the use of interfacial shear driven by the ionic wind generated at the tip of singular electrodes raised to sufficiently large voltages that result in atmospheric discharge (Yeo *et al.*, 2006a,b; Arifin *et al.*, 2007; and Hou *et al.*, 2007). Besides the requirement for extremely high voltages and nonplanar electrodes, such schemes are also considerably more inefficient given the need for interfacial shear to drive liquid recirculation in the bulk, unlike in the present case wherein the acoustic energy from the SAW is directly transmitted as bulk sound waves in the liquid, which, in turn, drives the streaming. This is reflected in the concentration time scales, which are on the order 1–10 s compared to 10^2–10^3 s with discharge-driven flows. Moreover, it is also possible to obtain much longer range convection with the SAW given that this is governed by the attenuation length of the sound wave in the fluid, which can hence be tuned with the applied SAW frequency; for particle concentration, the requirement is simply that the attenuation length is below that of the drop dimension (Destgeer *et al.*, 2016).

In this study, we investigate the possibility of enhancing the acoustic streaming velocity through the use of an amplitude modulation scheme and subsequently demonstrate that this can be exploited to significantly improve the efficiency of concentrating microparticles and also micromixing atop the SAW device. A similar strategy was previously employed by Rajapaksa *et al.* (2014) to enhance the rate of atomization for nebulizer applications, in which it was shown that a twofold increase in the rate with the same input power is attainable. Unlike SAW atomization, however, which requires high intensity acoustic fields (commensurate with acoustic Reynolds numbers (Rozenberg, 1971) $\mathrm{Re_A} \equiv \rho U_1 \lambda_f/(2\pi b) \geq 1$, where U_1 the acoustic particle velocity, λ_f the acoustic wavelength in the liquid and $b = 4\mu/3 + \mu_\mathrm{B}$, in which μ and μ_B are the shear and bulk viscosities of the liquid, respectively) to destabilize the air–liquid interface,

our focus in this work is confined to weaker acoustic fields ($Re_A < 1$) wherein the deformation of capillary waves at the air–interface is negligible and hence the acoustic energy supplied to the fluid by the SAW is largely converted to driving the acoustic streaming recirculation within the drop. In this respect, the amplitude modulation is expected to assume a completely distinct role compared to that for SAW atomization where the role of the kHz order modulation was predominantly applied to excite bulk vibration modes of the drop associated with capillary–inertia resonance (Blamey *et al.*, 2013) in order to destabilize its interface.

II. EXPERIMENT

The SAW device used in the study comprised a 128° rotated *Y*-cut *X*-propagating, single-crystal lithium niobate ($LiNbO_3$) piezoelectric substrate fabricated with a focusing elliptical single-phase unidirectional transducer (FE-SPUDT) (Shilton *et al.*, 2008) with 30 finger pairs (see Fig. 1) using standard UV photolithography. In particular, the FE-SPUDT was constructed from 750 nm thick aluminium atop a 4 nm thick chromium layer, both sputter deposited on the $LiNbO_3$ substrate. To generate the SAWs, a sinusoidal electric signal generated from a primary wavefunction generator (WF1966, NF Corporation, Japan) was amplified using a high frequency amplifier (25A250A, Amplifier Research, USA), and subsequently applied to the FE-SPUDT. The frequency of the electrical signal was set at 30.5 MHz in order to match the resonant frequency f_{SAW} of the FE-SPUDT, determined by the spacing of its fingers. For amplitude modulation, a secondary wavefunction generator (DG 1022, Rigol, China) was connected to the primary function generator; modulation frequencies of $f_m = 1$, 5, 10, 15, and 20 kHz were employed.

In order to quantify the total input electric power of the modulated signal to the SAW device, the modulation index (Frenzel, 2007) $m \equiv V_m/V_c$ was first calculated, in which $V_m = (V_{max} - V_{min})/2$ is the modulating signal voltage, $V_c = (V_{max} + V_{min})/2$ the carrier signal voltage, and V_{max} and V_{min} the maximum and minimum RMS voltages, respectively. The voltages were measured using a voltage probe (TPP 0201, Tektronix, USA) connected to an oscilloscope (TDS 2012C, Tektronix, USA). The total input electric power of the modulated signal can then be calculated (Frenzel, 2007) from $W_e = P_c(1 + m^2/2)$, in which $P_c = V_c I_c$ is the RMS power of the carrier signal and $I_c = (I_{max} + I_{min})/2$ the carrier signal current, wherein I_{max} and I_{min} are the maximum and minimum RMS currents, respectively, measured using an AC current probe (P6022, Tektronix, USA). We note that the SAW device was not designed to match the impedance of the source, i.e., a fraction of the input power is reflected back to the source due to the mismatch in the source and device impedances.

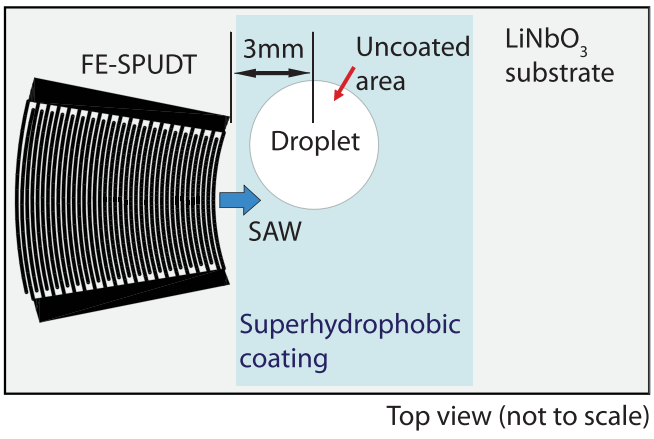

FIG. 1. Schematic illustration of the SAW device on which a focusing elliptical single-phase unidirectional transducer (FE-SPUDT) is patterned. The approximate location where the droplet is placed on the device to break the symmetry of the acoustic radiation into the liquid and hence to generate azimuthal recirculation within it is shown.

In each experiment, a controlled volume of deionized (DI) water was carefully pipetted onto the substrate. In order to generate the azimuthal recirculation necessary to drive particle concentration and micromixing in the droplet, the droplet is placed asymmetrically such that only a part of it lies in the SAW propagation path following the symmetry breaking procedure suggested in preceding studies (Shilton *et al.*, 2008 and Li *et al.*, 2007). In this case, the droplet was placed such that the center of the droplet is approximately 3 mm from the leading edge of the transducer, as illustrated in Fig. 1. In order to maintain its shape, the droplet is confined in a circular area by patterning a thin layer of superhydrophobic coating (NeverWet, Rustoleum, USA) on the substrate with a 5 mm diameter circular exclusion (bare surface) where the droplet is to be placed in order to prevent its spreading under the SAW excitation. The superhydrophobic modification was carried out by directly spraying two coating layers—a base coat and a top coat—on the SAW device, allowing 30 min of drying time at room temperature in between the application of each layer. Prior to spraying, the 5 mm diameter circular exclusion area was masked using tape. The experiments in Sections II A, II B and II C were then conducted to first measure the acoustic streaming velocity within the droplet and hence to subsequently quantify the effectiveness of the amplitude modulation in enhancing acoustic streaming and thus particle concentration and micromixing.

A. Enhancement in acoustic streaming

To investigate the relationship between the amplitude modulation frequency f_m and the acoustic streaming velocity U_{dc}, $\phi_p = 6\,\mu$m diameter fluorescently-tagged polystyrene spherical microparticles (Polysciences, USA) were suspended in deionized water droplets with volume $V_d = 5\,\mu\ell$ at a concentration of approximately 5%. We note here that the streaming velocities are insensitive to the particle size in the 1–10 μm range where the tracer particles are sufficiently large that Brownian diffusion effects can be neglected but sufficiently small such that their presence does not disrupt or influence the flow field. These tracer particles were then illuminated using a 480 nm fluorescence light source (AM4113t-GFBW, Dino-Lite, Taiwan) and their motion tracked using a high speed camera (M310, Phantom, USA) operating at 300 frames/s connected to an optical microscope (BX41M, Olympus, Japan) at 20× magnification. The particles were tracked using the supplied camera software (PCC 2.2, Phantom, USA) from which their average velocities can be determined, which is a good approximation of the acoustic streaming velocity U_{dc}. These velocity measurements were carried out for three different input powers W_e: 22 mW, 92 mW, and 156 mW. For each input power, different amplitude modulation frequencies f_m—1, 5, 10, 15, and 20 kHz—were examined. Additionally, the temperatures of the substrate and the droplet were measured using a thermal imager (TIM160, Micro-epsilon, Germany) at a record rate of 100 Hz.

B. Particle concentration efficiency

To demonstrate the efficiency of using amplitude modulation to improve the particle concentration process, we employ the same high speed imaging system to visualize the particle dynamics. More specifically, we determine the time required to concentrate the particles suspended in the droplet through a pixel intensity analysis (Mathematica 9.0, Wolfram, USA) of successive grayscale image frames acquired from the high speed video. The normalized standard deviation in the pixel intensity can be calculated by dividing the standard deviation of the pixel intensities for a given frame with respect to that for the first frame. The concentration time t_c can then be defined as the time required for the normalized standard deviation to reach a constant value (Shilton *et al.*, 2008 and Li *et al.*, 2007). The effects of three different sizes of fluorescent polystyrene microparticles, 6 μm, 10 μm, and 25 μm, used without further surface modification, in 5 μl deionized water droplets with the concentration held approximately at 5% were examined. For each particle size, the experiments were repeated using the different input powers and amplitude modulation frequencies specified above.

C. Micromixing efficiency

Finally, we demonstrate the use of amplitude modulation to improve the mixing process in the droplet. To observe the mixing process, a small amount of 1.5 μl dark blue food dye was pipetted onto a 6 μl glycerin droplet; the total volume of the droplet after addition of the dye is 7.5 μl. To minimize initial mixing due to convective currents that could arise during pipetting, high viscosity glycerin was used in this experiment instead of deionized (DI) water and the introduction of the dye to the droplet was carried out slowly and with care (Shilton *et al.*, 2008). The mixing process was then recorded using the same high speed camera system but with a high intensity bright-field illuminator (OSL, Thorlabs, USA). The normalized standard deviation in the pixel intensity was used to quantify the mixing performance by calculating a mixing efficiency; a value of 0 represents perfect mixing, whereas a value of 1 represents the no mixing case. In addition, an effective diffusivity D_{eff} can be approximated from a linear regression of the plot of the normalized standard deviation in the pixel intensity against time (Shilton *et al.*, 2008); the gradient of the slopes in the plots of the normalized standard deviation in the pixel intensity as a function of time is proportional to $-D/L^2$, in which D is the diffusivity and L the characteristic length scale of the droplet. The experiments were conducted for several different modulation frequencies (1, 5, and 15 kHz) and input powers (107, 165, and 264 mW).

III. NUMERICAL ANALYSIS

To gain qualitative insight on how the amplitude modulation leads to an intensification of the flow, we turn to a simplified two-dimensional numerical model for acoustic streaming, which consists of boundary layer streaming ($\mathcal{L} < \lambda_f$) and Eckart streaming ($\mathcal{L} > \lambda_f$), the latter arising due to dissipation of the sound energy as the SAW leaks into the droplet at the Rayleigh angle (Friend and Yeo, 2011 and Yeo and Friend, 2014); $\mathcal{L}$ is the characteristic length scale of the streaming. The governing equations are the continuity equation (Morse and Ingard, 1986 and Nyborg, 1988)

$$\frac{\partial \rho}{\partial t} + \nabla \cdot \rho \mathbf{u} = 0, \tag{1}$$

the Navier-Stokes equation

$$\rho \frac{\partial \mathbf{u}}{\partial t} + \rho(\mathbf{u} \cdot \nabla)\mathbf{u} = -\nabla p + \mu \nabla^2 \mathbf{u} + \left(\mu_{\text{B}} + \frac{\mu}{3}\right)\nabla \nabla \cdot \mathbf{u}, \tag{2}$$

and a thermodynamic relationship describing the adiabatic process (Beyer, 1988 and Rozenberg, 1971)

$$p - p_0 = A\frac{\rho - \rho_0}{\rho_0} + \frac{B}{2}\left(\frac{\rho - \rho_0}{\rho_0}\right)^2, \tag{3}$$

where p is the pressure, $\mathbf{u} = (u, w)$ the fluid velocity, t the time, $A = \rho_0 c_0^2$ and $B = \rho^2(\partial c^2/\partial \rho)$ in which c is the sound speed. The subscript "0" denotes the fluid properties at equilibrium and c_0 is the isentropic sound speed for small-signal amplitudes. Under the assumption of infinitesimally small amplitude waves, the method of successive approximations can be employed to linearize the equations above wherein a perturbation expansion in the small parameter $\epsilon = U/c_0 \ll 1$, where U is the characteristic acoustic particle velocity, is imposed on the pressure and density fields (Morse and Ingard, 1986 and Nyborg, 1988)

$$\mathbf{u} = \mathbf{u}_0 + \epsilon \mathbf{u}_1 + \epsilon^2 \mathbf{u}_2 + \cdots, \tag{4}$$

$$p = p_0 + \epsilon p_1 + \epsilon^2 p_2 + \cdots, \tag{5}$$

$$\rho = \rho_0 + \epsilon\rho_1 + \epsilon^2\rho_2 + \cdots \tag{6}$$

By substituting Eqs. (4)–(6) into Eqs. (1)–(3), the first-order (acoustic field) approximations to these equations can then be written as (Morse and Ingard, 1986 and Nyborg, 1988)

$$\frac{\partial\rho_1}{\partial t} + \rho_0\nabla\cdot\mathbf{u}_1 = 0, \tag{7}$$

$$\rho_0\frac{\partial\mathbf{u}_1}{\partial t} = -\nabla p_1 + \mu\nabla^2\mathbf{u}_1 + \left(\mu_B + \frac{\mu}{3}\right)\nabla\nabla\cdot\mathbf{u}_1, \tag{8}$$

and

$$p_1 = c_0^2\rho_0. \tag{9}$$

Given the assumption of small amplitude deformations, we note that these linear equations are strictly applicable only when the acoustic field is weak, i.e., $\mathrm{Re}_A < 1$.

At the next order, the fluid motion consists of a superposition of the steady-state and time-oscillating harmonic flows. Time averaging all terms, the second-order (acoustic streaming) approximation to Eqs. (4)–(6) become

$$\nabla\cdot(\rho_0\mathbf{u}_2) + \nabla\cdot\langle\rho_1\mathbf{u}_1\rangle = 0, \tag{10}$$

$$\rho_0\frac{\partial\mathbf{u}_{dc}}{\partial t} + \left\langle\rho_1\frac{\partial\mathbf{u}_1}{\partial t}\right\rangle + \rho_0\langle\mathbf{u}_1\cdot\nabla\mathbf{u}_1\rangle = -\nabla p_{dc} + \mu\nabla^2\mathbf{u}_{dc} + \left(\mu_B + \frac{\mu}{3}\right)\nabla\nabla\cdot\mathbf{u}_{dc}, \tag{11}$$

and

$$p_{dc} = \frac{1}{2}\frac{c_0^2}{\rho_0}\left[\frac{B}{A}\langle\rho_1^2\rangle + 2\rho_0\rho_{dc}\right], \tag{12}$$

wherein $\langle\cdot\rangle$ refers to time averaging of the terms within and the subscript "dc" refers to the steady-state terms. Combining Eqs. (10) and (11) and separating the first-order quantities from the remaining terms, we obtain an expression for the steady-state acoustic streaming force density (Morse and Ingard, 1986 and Nyborg, 1988)

$$\mathbf{F}_{dc} = \rho_0\frac{\partial\mathbf{u}_{dc}}{\partial t} + \nabla p_{dc} - \mu\nabla^2\mathbf{u}_{dc}, \tag{13}$$

and

$$\mathbf{F}_{dc} = -\left\langle\rho_1\frac{\partial\mathbf{u}_1}{\partial t}\right\rangle - \rho_0\langle\mathbf{u}_1\cdot\nabla\mathbf{u}_1\rangle - \frac{1}{\rho_0}\left(\mu_B + \frac{\mu}{3}\right)\langle\nabla\nabla\cdot(\rho_1\mathbf{u}_1)\rangle. \tag{14}$$

Equations (7)–(9) can then be solved to model the acoustic wave propagation in the fluid, whereas Eqs. (12)–(14) can be solved to model the acoustic streaming (Tan *et al.*, 2010). A finite difference time domain numerical scheme (Schröder and Scott, 2000) was used to obtain solutions to these equations on a two-dimensional rectilinear ($x-y$) computational domain (Fig. 2) of dimension 4 mm × 2 mm; the longer axis constituting the y-direction. Given a grid size $\Delta x = \Delta y = 2\,\mu$m, approximately 24 computational nodes are assigned to a wavelength λ_f. On the surface of the acoustic radiator ($0 \le x \le 4$ mm and $y = 0$), a sinusoidal boundary condition for the first-order instantaneous acoustic velocity is imposed to simulate the SAW propagation on the $LiNbO_3$ substrate (Frenzel, 2007)

$$u_1 = [u_{SAW}\sin(\theta_{SAW} - \pi/2) + u_m\sin\theta_m\sin(\theta_{SAW} - \pi/2)]\exp(-x/\alpha_{SAW}), \tag{15}$$

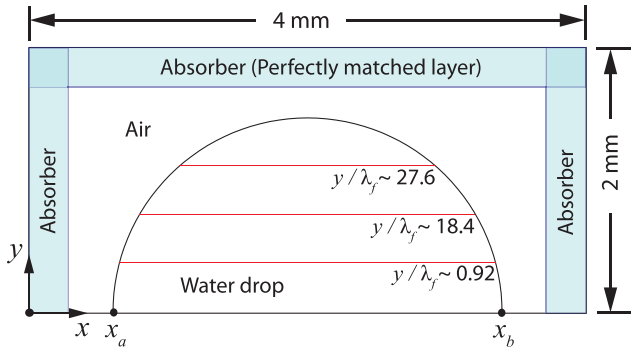

FIG. 2. A two-dimensional schematic of the computational domain used to model the propagation of the acoustic waves. The drop is assumed to be a hemisphere of diameter $D_d = 3.6$ mm. The boundary condition that simulates the SAW propagation is applied from x_a to x_b. The average acoustic streaming velocity is computed at three different heights: $y \approx 0.92\lambda_f$, $18.4\lambda_f$, and $27.6\lambda_f$.

$$w_1 = (w_{\mathrm{SAW}} \sin\theta_{\mathrm{SAW}} + w_m \sin\theta_m \sin\theta_{\mathrm{SAW}}) \exp(-x/\alpha_{\mathrm{SAW}}), \tag{16}$$

as shown in Figure 3(a). $\theta_{\mathrm{SAW}} = \omega_{\mathrm{SAW}} t - k_{\mathrm{SAW}} x$, $\theta_m = \omega_m t - k_m x$, $k_{\mathrm{SAW}} = \omega_{\mathrm{SAW}}/c_{\mathrm{SAW}}$, $k_m = \omega_m/c_{\mathrm{SAW}}$, $\omega_{\mathrm{SAW}} = 2\pi f_{\mathrm{SAW}}$, and $\omega_m = 2\pi f_m$; c_{SAW} being the velocity of the SAW on the $LiNbO_3$ substrate. $u_{\mathrm{SAW}} = w_{\mathrm{SAW}}$ represents the peak amplitude of the SAW and $u_m = w_m$ the peak amplitude of the modulation wave; the modulation index is thus approximated from $m \equiv u_m/u_{\mathrm{SAW}} = w_m/w_{\mathrm{SAW}}$. To allow for the attenuation of the SAW along the substrate surface beneath the droplet due to leakage of its energy into the liquid, we have imposed a characteristic attenuation length (Shilton *et al.*, 2014 and Frommelt *et al.*, 2008a), which can be approximated as $\alpha_{\mathrm{SAW}}^{-1} \approx 0.45\lambda_{\mathrm{SAW}}[\rho_{\mathrm{SAW}} c_{\mathrm{SAW}}/(\rho_0 c_0)]$. The other three boundaries are approximated by perfectly matched layer conditions (Tan *et al.*, 2010, 2009; and Schröder and Scott, 2000). We note that at the low excitation powers used to drive micromixing and particle concentration, the deformation of the droplet interface is typically negligible and hence the motion of the air–liquid interface is not considered in the analysis. To ensure computational stability, the Courant criterion was adopted (Anderson, 1995).

Two distinct hydrodynamic forces—the streaming force within the viscous boundary layer of thickness (Morse and Ingard, 1986) $\delta_v \equiv (2\mu/\rho_0\omega)^{1/2}$ and that outside the boundary layer—are dominant in the flow within the droplet (Manor *et al.*, 2015 and Rezk *et al.*, 2014). Given that the characteristic length scale of the droplet $\mathcal{L}_d \sim 10^{-3}$ m $\gg \delta_v \sim 10^{-7}$ m, it is possible to assume that the streaming force within the viscous boundary layer is insignificant as compared

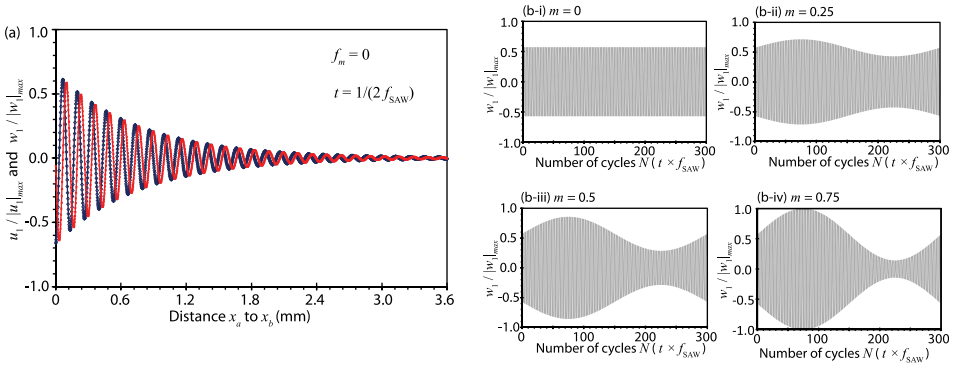

FIG. 3. (a) Instantaneous velocity boundary condition (Eqs. (15) and (16)) in the x-direction u_1 (◇) and the y-direction w_1 (×) imposed on the substrate surface ($y = 0$) from x_a to x_b (see Fig. 2) in the absence of amplitude modulation ($f_m = 0$). The attenuation of the SAW along the substrate surface is approximated as $\exp(-x/\alpha_{\mathrm{SAW}})^{-1}$, where $\alpha_{\mathrm{SAW}}^{-1}$ is the characteristic SAW attenuation length. (b) Variation in the acoustic velocity in the y-direction w_1 at $x = x_a$ as a function of the number of cycles for different modulation indices: (i) $m = 0$ (no modulation), (ii) $m = 0.25$, (iii) $m = 0.5$, and (iv) $m = 0.75$; the frequency of the SAW is $f_{\mathrm{SAW}} = 30$ MHz and the modulation frequency is $f_m = 100$ kHz.

to that outside the boundary layer, and, as such, adopt larger grid spacings than the boundary layer thickness, i.e., $\Delta x = \Delta y \gg \delta_v$, to reduce computational cost. We note that the acoustic streaming outside the boundary layer is associated with thermoviscous attenuation, which, for the case of a plane sound wave propagating in an unbounded medium and for $\omega\tau_s \ll 1$, where $\tau_s = b/(\rho_0 c^2)$ is the relaxation time (Kinsler *et al.*, 2000), is characterised by an attenuation coefficient (Hamilton *et al.*, 1998) defined by $\alpha \approx b\omega^2/(2\rho_0 c_0^3)$, where $b = 4\mu/3 + \mu_B$, in which μ and μ_B are the shear and bulk viscosities of the liquid.

IV. RESULTS AND DISCUSSION

A. Enhancement in acoustic streaming

It can be seen from Fig. 3(b-ii–iv), which examines the acoustic velocity along the y-direction at a fixed arbitrary location $x = x_a$, that the maximum acoustic velocity amplitude increases, whereas the minimum acoustic velocity amplitude decreases in the presence of amplitude modulation ($m > 0$), and that this change in the velocity amplitude is sensitive to the modulation index m: increasing m leads to larger maximum acoustic velocity amplitudes and smaller minimum acoustic velocity amplitudes. At the same location ($x = x_a$), it is then possible to evaluate the change in the amplitudes of the maximum and minimum acoustic velocities for different modulation indices, from which we observe a linear dependence of their magnitudes $|U_1| = (u_1^2 + w_1^2)^{1/2}$ on the modulation index (Fig. 4(a)); note that for $f_m = 100$ kHz, the maximum acoustic velocity amplitude occurs at $t = (1/4)f_m^{-1}$ (or $n = 75$), whereas the minimum acoustic velocity amplitude occurs at $t = (3/4)f_m^{-1}$ (or $n = 225$), $n = tf_{SAW}$ being the number of cycles. Given that the steady-state acoustic streaming velocity scales as the square of the instantaneous acoustic velocity, i.e., $U_{dc} \sim U_1^2$, which we estimate as the average of the squared acoustic velocity amplitude at the maximum and minimum points, i.e., $|U_1|^2_{avg} = (|U_1|^2_{t=1/(4f_m)} + |U_1|^2_{t=3/(4f_m)})/2$, it can be seen from Fig. 4(b) that the acoustic streaming velocity increases with increasing modulation index as $U_{dc} \sim 10^m$.

Figure 5 shows the instantaneous acoustic pressure p_1 within a $D_d = 3.7$ mm droplet, which is slightly smaller than that used in the experiment $D_d \approx 5$ mm due to limitations in the domain size we are able to simulate, at $t = 100f_{SAW}^{-1}$ ($n = 200$) and $t = 300f_{SAW}^{-1}$ ($n = 300$), arising as a consequence of leakage of the SAW energy from the substrate into the droplet, when no amplitude modulation is present ($m = 0$). It can be seen that strong standing waves inside the droplet arise after 300 cycles (Fig. 5(b)), consistent with the results shown by Brunet *et al.* (2010). Despite the simplicity of the approximate model, the computed magnitude of the steady-state streaming velocity $U_{dc,}$ on the order 10^{-3} m/s, is consistent with that in the experiments in Fig. 7. More importantly, the intensification of the acoustic streaming in the droplet with amplitude modulation, i.e., increasing m, can be qualitatively captured by averaging the magnitude of

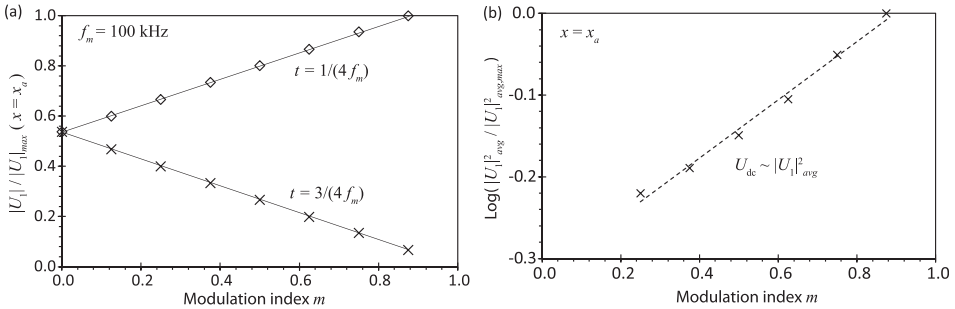

FIG. 4. (a) Change in the magnitude of the acoustic velocity $|U_1| = (u_1 + w_1)^{1/2}$ at $x = x_a$ for different modulation indices m over two different time cycles: $t = 1/(4f_m)$ representing the maximum amplitude (◇) and $t = 3/(4f_m)$ representing the minimum amplitude (×). Note that $m = 0$ represents the case where amplitude modulation is absent. The trendlines were added to aid visualization. (b) Average squared values of the acoustic velocity amplitude $|U_1|^2_{avg} = (|U_1|^2_{t=1/(4f_m)} + |U_1|^2_{t=3/(4f_m)})/2$ at $x = x_a$ at the two different time cycles for different modulation indices. The dotted line represents a least square fit ($R^2 = 0.991$) and suggests that $U_{dc} \sim 10^m$.

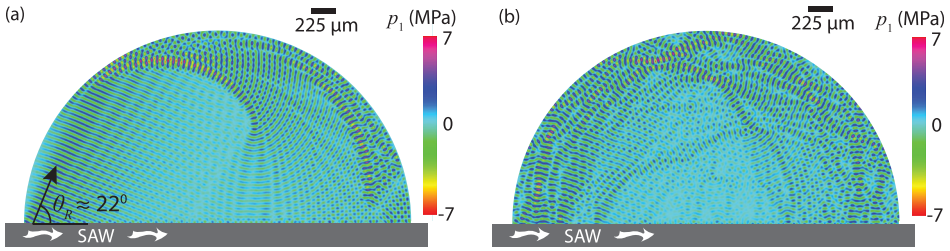

FIG. 5. Acoustic pressure field p_1 in a droplet of diameter $D_d = 3.6$ mm ($\gg \lambda_f \approx 49\,\mu$m) at time (a) $t = 100 f_{\mathrm{SAW}}^{-1}$ and (b) $t = 300 f_{\mathrm{SAW}}^{-1}$ arising from sound wave transmission into the liquid as a consequence of the SAW propagation along the substrate beneath it; $f_{\mathrm{SAW}} = 30$ MHz and $m = 0$ (no amplitude modulation). It can be seen in (a) that the sound wave leaks into the droplet at the Rayleigh angle $\theta_R = \sin^{-1}(c_0/c_{\mathrm{SAW}}) \approx 22^\circ$ (for water $c_0 \approx 1480$ m/s and for $LiNbO_3$ substrate $c_{\mathrm{SAW}} \approx 3990$ m/s) and that strong standing waves are formed in the droplet at $t = 300 f_{\mathrm{SAW}}^{-1}$.

the acoustic streaming velocity $U_{\mathrm{dc}} = (u_{\mathrm{dc}}^2 + w_{\mathrm{dc}}^2)^{1/2}$ at three different heights $y/\lambda_f = 9.2$, 18.4, and 27.6 as shown in Fig. 6 for a modulation frequency $f_m = 100$ kHz, which we shall observe are consistent with that observed in the experiments in Fig. 7(a) ($f_m = 100$ kHz and $f_{\mathrm{SAW}} = 30.5$ MHz); the relationship obtained from the experimental results, i.e., $U_{\mathrm{dc}} \sim 10^m$, is consistent with the numerical results (Fig. 6). Additionally, we also observe in Fig. 6 that the enhancement in the streaming velocity becomes increasingly prominent the further the distance from the substrate surface, i.e., larger y/λ_f, suggesting that the increase in streaming velocity with amplitude modulation is more significant for larger droplets.

Figure 7(b) shows that the acoustic streaming velocity increases by approximately 30% in experiments with low frequency amplitude modulation ($f_m = 1$ kHz) compared to the case in which the signal was not modulated ($f_m = 0$). Further monotonic increases in the acoustic streaming velocity can then be obtained by increasing the amplitude modulation frequency until about 10 kHz, after which any further changes in the streaming velocity become insignificant. The reduction in the streaming velocity when $f_m < 10$ kHz can be attributed to the increase in the modulation wavelength $\lambda_m/4$ beyond the thermoviscous attenuation length α^{-1}, i.e., $\lambda_m/4 > \alpha^{-1}$, which results in a decrease in the acoustic streaming velocity until it approaches the value for the streaming velocity in the absence of amplitude modulation ($f_m = 0$). This can be seen more clearly when one notes that the modulation wavelength $\lambda_m/4$ at $f_m = 10$ kHz, which is approximately 37 mm, becomes comparable to the attenuation length $\alpha^{-1} \approx 40$ mm for

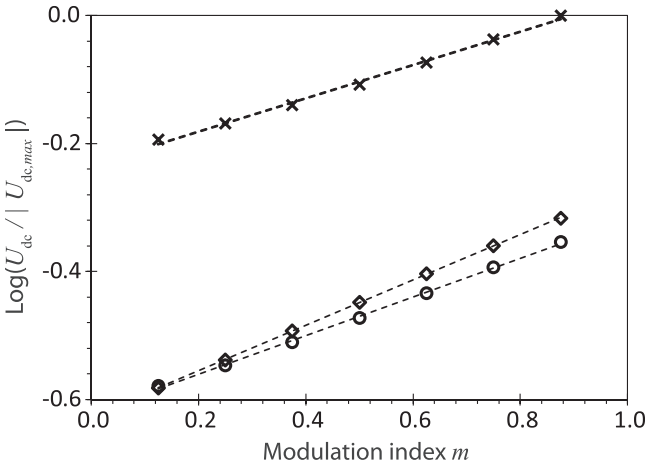

FIG. 6. Results from the numerical simulation showing the relationship between the average acoustic streaming velocity $U_{\mathrm{dc}} = (u_{\mathrm{dc}}^2 + w_{\mathrm{dc}}^2)^{1/2}$ and the modulation index m at three different heights in the droplet: $y \approx 9.2\lambda_f$ (◇), $18.4\lambda_f$ (○), and $27.6\lambda_f$ (×) (see Fig. 2). The modulation frequency is fixed at $f_m = 100$ kHz and $m = 0$ represents the case where amplitude modulation is absent. The dotted lines represent least square fit—$R^2 = 1.000$ (◇), $R^2 = 0.999$ (○), and $R^2 = 0.996$ (×)—and suggests that $U_{\mathrm{dc}} \sim 10^m$.

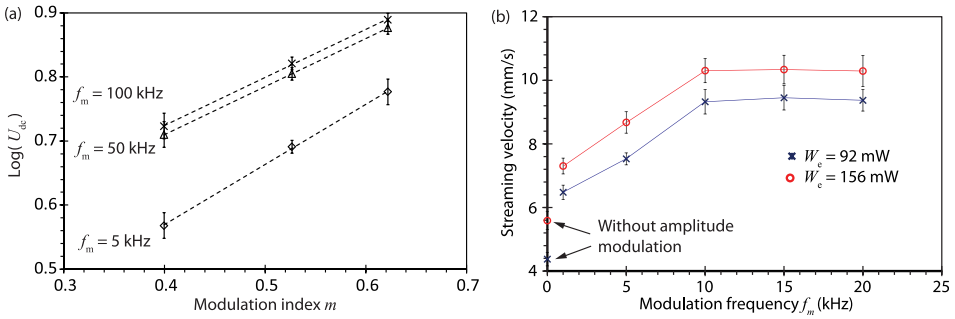

FIG. 7. (a) Experimental results depicting the relationship between the acoustic streaming velocity U_{dc} and the modulation index m at three different modulation frequencies $f_m = 5$ kHz (◇), $f_m = 50$ kHz (△), and $f_m = 100$ kHz (×) in a 5 μl droplet suspended with 6 μm particles. The power is fixed at $W_e = 20$ mW. The dotted lines represent least square fit—$R^2 = 0.999$ (◇), $R^2 = 1.000$ (△), and $R^2 = 0.999$ (×)—and suggests that $U_{dc} \sim 10^m$, consistent with that shown in Fig. 6. (b) Experimental results showing the relationship between the acoustic streaming velocity U_{dc} and the modulation frequency f_m at two different powers $W_e = 92$ mW (×) and $W_e = 156$ mW (○) in a 5 μl droplet suspended with 6 μm particles. The case $f_m = 0$ represents the condition in the absence of amplitude modulation. The piezoelectric substrate is excited by 30.5 kHz SAWs. Error bars indicate a ±2 standard deviation (95% confidence level) from the mean. Trendlines in (b) were added to aid visualization.

$f_{SAW} = 30.5$ MHz. Overall, we find a maximum increase in U_{dc} of up to 60% with amplitude modulation frequencies up to 20 kHz.

To ensure that the higher peak of modulated acoustic waves (see Fig. 3) does not drastically increase the temperature (as a consequence of viscous dissipation of the sound wave in the liquid), we measured the droplet temperature as well as the substrate surface temperature, both initially and after 5 min of excitation, under different conditions. As can be seen in the temperature measurements tabulated in Table I, the surface temperature of the substrate appears to be almost identical regardless of whether amplitude modulation is employed or not, suggesting that it poses no significant effect on heat generation within the substrate, which is to be expected since viscous dissipation only occurs in the liquid when sound waves, generated as a consequence of leakage of energy from the SAW into the liquid, propagate through it. In contrast, we note that amplitude modulation causes the droplet to be heated by 7° to 8 °C—1° to 2 °C lower than that in the absence of amplitude modulation where temperature increases of 9 °C for the same input power and droplet volume are measured. This reduction in droplet temperature with amplitude modulation can be attributed to the increase in convective heat transport as a result of the higher streaming velocities. In any case, such a reduction in temperature, while modest, is an advantage, especially where biological assays are employed in the SAW microfluidic platforms since heating can have adverse implications on the retention of the structural and functional viabilities of these biomolecules (Yeo and Friend, 2014).

B. Particle concentration efficiency

The particle concentration process in a 5 μl droplet driven by the SAW microcentrifugation flow is illustrated in Fig. 8(a) wherein the time t_c it takes for microparticles of various dimensions to concentrate at the center of the droplet as a function of the input power W_e and at different modulation frequencies is reported in Figs. 8(b)–8(d). It can be seen in all cases that the

TABLE I. Measured substrate surface (in the absence of the droplet) and droplet temperatures, initially (T_0) and after 5 min (T_5), both in the absence ($f_m = 0$ kHz) and in the presence ($f_m = 15$ kHz) of amplitude modulation. The input power is held constant at 156 mW. Where a droplet is present, its volume is held constant at 5 μl.

	Substrate surface		Droplet	
f_m (kHz)	0	15	0	15
T_0 (°C)	22.9 ± 0.1	22.9 ± 0.2	21.0 ± 0.1	21.0 ± 0.2
T_5 (°C)	29.4 ± 0.5	29.5 ± 0.3	30.1 ± 0.3	28.2 ± 0.1

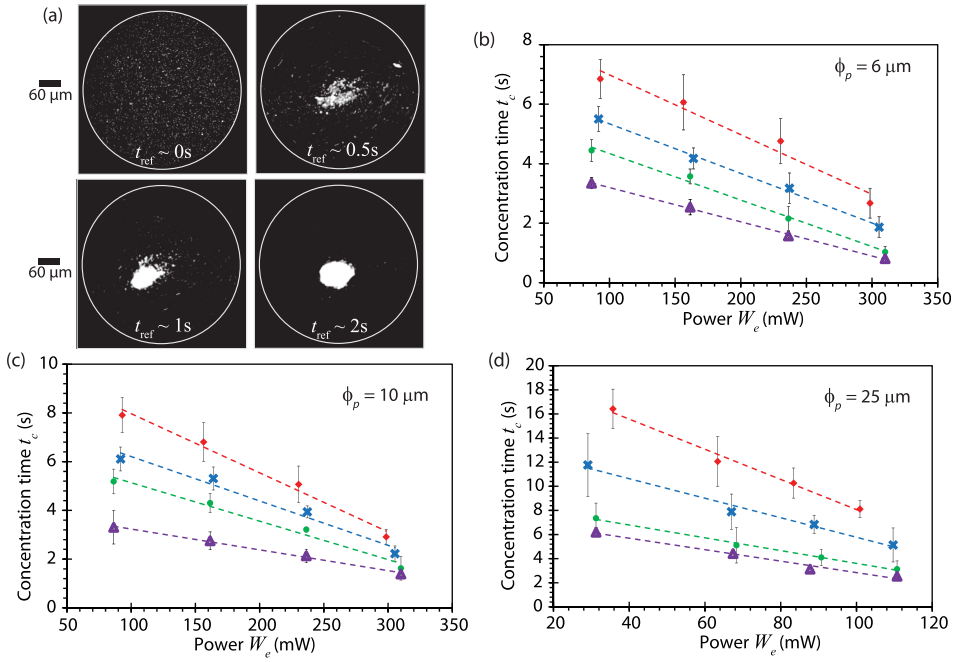

FIG. 8. (a) Successive time-sequence images showing the concentration of $\phi_p = 6\,\mu$m diameter particles suspended in a 5 μl water droplet excited at $W_e \approx 300$ mW when subjected to amplitude modulation at a frequency of $f_m = 1$ kHz. Measured concentration times for (b) $\phi_p = 6\,\mu$m, (c) $\phi_p = 10\,\mu$m, and (d) $\phi_p = 25\,\mu$m diameter particles suspended in a 5 μl water droplet excited at different powers W_e and under different amplitude modulation conditions: $f_m = 0$ (without modulation) (◇), $f_m = 1$ kHz (×), $f_m = 5$ kHz (●), and $f_m = 15$ kHz (△). Error bars indicate a ±2 standard deviation (95% confidence level) from the mean. Trendlines were added to aid visualization.

concentration time decreases significantly as the amplitude modulation frequency is increased, as expected given the increase in the acoustic streaming velocity and, as a consequence, the drag and the shear rate. The former is an important consideration if the particle concentration occurs in the bulk due to secondary meridional convection (Raghavan *et al.*, 2010), whereas the latter is important in the shear-induced migration dominant mechanism responsible for particle concentration on the free surface of the droplet (Shilton *et al.*, 2008 and Li *et al.*, 2007), which is the prevalent mechanism in the present case. This can be seen by the linear relationship between the concentration time and the particle size scaling (see Fig. 9), consistent with that

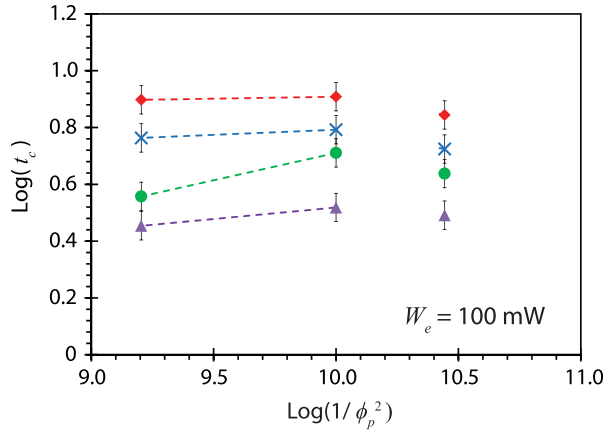

FIG. 9. Relationship between the concentration time t_c interpolated from the data in Fig. 8 as a function of the particle dimension $1/\phi_p^2$ scaling for a fixed input power (100 mW), under different amplitude modulations condition: $f_m = 0$ (without modulation) (◇), $f_m = 1$ kHz (×), $f_m = 5$ kHz (●), and $f_m = 15$ kHz (△). Error bars indicate a ±2 standard deviation (95% confidence level) from the mean.

for shear-induced migration into a vortex (Li *et al.*, 2007) $t_c \sim D_d^2/(\phi_p^2 \dot{\gamma} \psi)$, in which $\dot{\gamma}$ is the shear rate, and ψ the local particle volume fraction in the vortex. The concentration time t_c for $\phi_p = 6\,\mu$m particles does not fit the $1/\phi_p^2$ trend; as reported by Li *et al.* (2007), this is due to the aggregation of small particles ($\phi_p < 10\,\mu$m), resulting in larger effective particle sizes and hence a decrease in the concentration time.

With increasing amplitude modulation frequencies, it can be seen in all cases from Fig. 8 that the improvement in particle concentration speed, however, diminishes. This is because the increase in acoustic streaming velocities begins to taper beyond approximately 10 kHz in Fig. 7(b). For a fixed input power of 100 mW, we observe the reduction in the particle concentration time between the case of no amplitude modulation ($f_m = 0$ kHz) and modulation at 15 kHz to be 50%, 58%, and 69% for $\phi_p = 6\,\mu$m, 10 μm, and 25 μm microparticles, respectively.

Interestingly, we note that particles with sufficiently large dimensions, which would not have concentrated without amplitude modulation since the shear-induced drag is insufficient to overcome the acoustic radiation force which expels the particles to the droplet periphery (Rogers *et al.*, 2010), are able to concentrate when amplitude modulation is imposed. A simple explanation is that the drag force for a given particle size increases linearly with the acoustic streaming velocity, which is enhanced by a factor of two or three under amplitude modulation of the signal, as observed in Fig. 7(b). On the other hand, the increase in the acoustic radiation pressure which opposes the drag force is increased marginally when the kHz order modulation is imposed over the MHz order SAW due to the fourth power scaling of the radiation force with frequency (King, 1934). As such, the crossover particle size (Rogers *et al.*, 2010) above which particles no longer concentrate in the centre of the droplet significantly shifts to much larger particle sizes when amplitude modulation is imposed, thus facilitating the concentration of particles with much larger dimensions. It then follows that amplitude modulation therefore forms a useful strategy to circumvent the particle size limitation when concentration is desired, without necessitating a change in the SAW frequency. Dynamic concentration and expulsion of

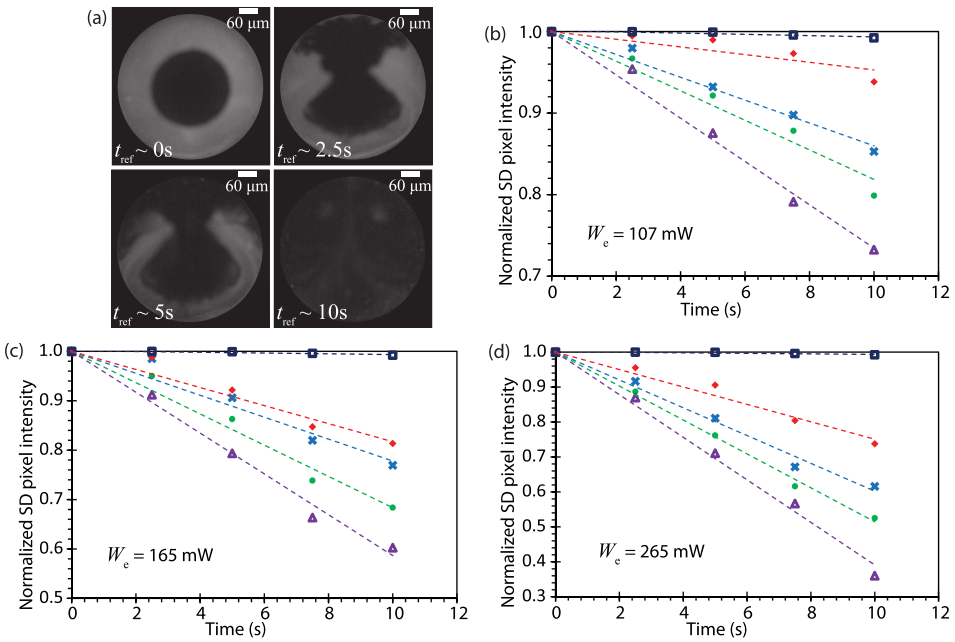

FIG. 10. (a) Successive time-sequence images showing the mixing progress of 1.5 μl of dye into a 6 μl glycerine droplet excited at $W_e = 265$ mW when subjected to amplitude modulation at a frequency of $f_m = 15$ kHz (the droplet circumference is delineated by the circles in the images). Normalized standard deviation in the pixel intensity to quantify the efficiency of mixing 1.5 μl of dye into a 5 μl glycerine droplet for three different input powers: (b) $W_e = 107$ mW, (c) $W_e = 165$ mW, and (d) $W_e = 265$ mW, and various modulation frequencies: $f_m = 0$ (without modulation) (◇), $f_m = 1$ kHz (×), $f_m = 5$ kHz (●), and $f_m = 15$ kHz (△). Trendlines were added to aid visualization.

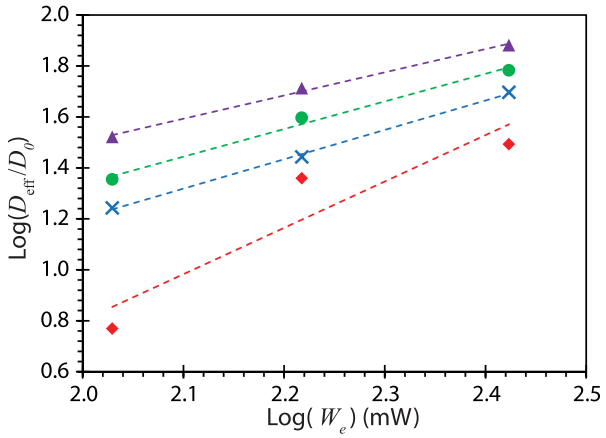

FIG. 11. Effect of the input power W_e on the mixing enhancement, approximated as the ratio of the effective diffusivity D_{eff} to the diffusivity due to pure diffusional mixing D_0 in the absence of SAW-driven convection. Four different conditions were examined: $f_m = 0$ (without modulation) (◇), $f_m = 1$ kHz (×), $f_m = 5$ kHz (●), and $f_m = 15$ kHz (△).

the particles can also be obtained by switching on and off the amplitude modulation, thus constituting a very simple but yet powerful tool for selective particle manipulation.

C. Micromixing efficiency

Figure 10(a) shows sequential images illustrating the mixing process under SAW excitation while Figs. 10(b)–10(d) reports the normalized standard deviation in the pixel intensity from which the efficiency of mixing of a 1.5 μl dye into the 6 μl glycerine droplet can be determined. After 10 s, the improvement in mixing efficiency between the $f_m = 0$ (no modulation) and $f_m = 15$ kHz cases is approximately 22%, 26%, and 51% when the input power is $W_e = 107$, 165, and 265 mW, respectively, demonstrating that significant improvement in the micromixing (lower normalized standard deviation) can be achieved with amplitude modulation, due to the larger acoustic streaming velocities and hence stronger convection within the droplet. Given that the slopes of the curves are proportional to $-D/\mathcal{L}_d^2$, the mixing enhancement due to the acoustic streaming induced convection can be approximated by the ratio between an effective diffusivity due to the SAW-driven convective-mixing D_{eff} to the diffusivity in its absence D_0 (Shilton *et al.*, 2008). Figure 11 shows a comparison of the mixing enhancement as a function of the input power for the different modulation frequencies. It is then possible to compare the effectiveness of mixing afforded by each modulation frequency through a single power law $(D_{\text{eff}}/D_0) \sim W_e^n$: $n = 1.82$ for $f_m = 0$ (without modulation), $n = 1.15$ for $f_m = 1$ kHz, $n = 1.08$ for $f_m = 5$ kHz, and $n = 0.91$ for $f_m = 15$ kHz.

V. CONCLUSIONS

In this work, we have demonstrated a simple technique to increase the acoustic streaming velocity in SAW droplet microfluidic platforms via amplitude modulation, thus reducing the power requirement which is crucial in the development of a portable integrated microfluidic platform. Unlike previous attempts in which an amplitude modulation scheme was employed under strong acoustic field intensities ($\text{Re}_A \geq 1$) to induce capillary wave destabilization and breakup for liquid atomization (Rajapaksa *et al.*, 2014), the work here focuses on systems with low acoustic field intensities ($\text{Re}_A < 1$) where interfacial deformation is negligible. In particular, the acoustic streaming velocity is observed to intensify by increasing the modulation index, which results in larger peak acoustic-velocity amplitudes of the modulated SAWs; from our numerical simulations, we expect this increase in streaming velocity to become more significant with larger droplets. Increasing the modulation frequency is also observed to produce a similar enhancement effect: a 30% enhancement in the streaming velocity is observed with an amplitude modulation frequency of 1 kHz, increasing to approximately 60% at 10 kHz for $f_{\text{SAW}} = 30$ MHz. The enhancement,

however, is observed to diminish when the quarter-wavelength associated with the modulation frequency becomes comparable and subsequently shorter than the thermoviscous attenuation length, i.e., $\lambda_m/4 < \alpha^{-1}$, at increasing modulation frequencies; beyond approximately $f_m \approx 10\,\text{kHz}$, no further increases in the streaming velocity were observed. We further note that any enhancement in the acoustic streaming with amplitude modulation is accompanied by a modest reduction in the droplet temperature, which is a further advantage particularly for biomicrofluidic applications. Such intensification in acoustic streaming with amplitude modulation is also seen to translate into faster and more efficient microcentrifugation-driven particle concentration, reducing the time taken to concentrate particles in the centre of the droplet between 50% and 70% depending on the particle size. Similarly, the mixing efficiency in the droplet is observed to improve by approximately 50% with the amplitude modulation scheme.

ACKNOWLEDGMENTS

M.K.T. gratefully acknowledges funding for this work from the Fundamental Research Grant Scheme, Ministry of Higher Education Malaysia, through Project Grant No. FRGS/1/2015/SG02/MUSM/03/1. L.Y.Y. is supported by a Future Fellowship from the Australian Research Council under Grant No. FT130100672.

Anderson, J. D., *Computational Fluid Dynamics: The Basics with Application* (McGraw-Hill, 1995), p. 261.
Ang, K. M., Yeo, L. Y., Friend, J. R., Hung, Y. M., and Tan, M. K., J. Aerosol Sci. **79**, 48 (2015).
Arifin, D. R., Friend, J. R., and Yeo, L. Y., Biomicrofluidics **1**, 014103 (2007).
Baudoin, M., Brunet, P., Matar, O. B., and Herth, E., Appl. Phys. Lett. **100**, 154102 (2012).
Beyer, R. T., *Nonlinear Acoustics: The Parameter B/A*, edited by M. F. Hamilton and D. T. Blackstock (Academic Press, 1988), pp. 25–40.
Blamey, J., Yeo, L. Y., and Friend, J. R., Langmuir **29**, 3835 (2013).
Bourquin, Y., Reboud, J., Wilson, R., Zhang, Y., and Cooper, J. M., Lab Chip **11**, 2725 (2011).
Brunet, P., Baudoin, M., Matar, O. B., and Zoueshtiagh, F., Phys. Rev. E **81**, 036315 (2010).
Chen, Y., Li, S., Gu, Y., Li, P., Ding, X., Wang, L., McCoy, J. P., Levine, S. J., and Huang, T. J., Lab Chip **14**, 924 (2014).
Cheng, I.-F., Chang, H.-C., Hou, D., and Chang, H.-C., Biomicrofluidics **1**, 021503 (2007).
Cho, S. K., Zhao, Y., and Kim, C.-J., Lab Chip **7**, 490 (2007).
Collingnon, S., Friend, J., and Yeo, L., Lab Chip **15**, 1942 (2015).
Dentry, M. B., Yeo, L. Y., and Friend, J. R., Phys. Rev. E **89**, 013203 (2014).
Destgeer, G., Cho, H., Ha, B. H., Jung, J. H., Park, J., and Sung, H. J., Lab Chip **16**, 660 (2016).
Destgeer, G., Ha, B. H., Jung, J. H., Park, J., and Sung, H. J., Lab Chip **14**, 4665 (2014).
Destgeer, G., Ha, B. H., Park, J., Jung, J. H., Alazzam, A., and Sung, H. J., Anal. Chem. **87**, 4627 (2015).
Destgeer, G., Lee, K. H., Jung, J. H., Alazzam, A., Park, J., and Sung, H. J., Lab Chip **13**, 4210 (2013).
Destgeer, G. and Sung, H. J., Lab Chip **15**, 2722 (2015).
Dholakia, K., Reece, P., and Gu, M., Chem. Soc. Rev. **37**, 42 (2008).
Ding, X., Li, P., Lin, S.-C. S., Stratton, Z. S., Nama, N., Guo, F., Slotcavage, D., Mao, X., Shi, J., Costanzo, F., and Huang, T. J., Lab Chip **13**, 3626 (2013).
Frenzel, L., *Principles of Electronic Communication Systems* (McGraw-Hill, 2007).
Friend, J. R. and Yeo, L. Y., Rev. Mod. Phys. **83**, 647 (2011).
Frommelt, T., Gogel, D., Kostur, M., Talkner, P., Hänggi, P., and Wixforth, A., IEEE Trans. Ultrason., Ferroelectr., Freq. Control **55**, 2298 (2008a).
Frommelt, T., Kostur, M., Wenzel-Schafer, M., Talkner, P., Hanggi, P., and Wixforth, A., Phys. Rev. Lett. **100**, 034502 (2008b).
Glass, N. R., Shilton, R. J., Chan, P. P. Y., Friend, J. R., and Yeo, L. Y., Small **8**, 1881 (2012).
Hamilton, M. F., Il'inskii, Y. A., and Zabolotskaya, E. A., *Dispersion*, edited by M. F. Hamilton and D. T. Blackstock (Academic Press, 1998) pp. 151–175.
Harrison, H., Lu, X., Patel, S., Thomas, C., Todd, A., Johnson, M., Raval, Y., Tzeng, T.-R., Song, Y., Wang, J., Li, D., and Xuan, X., Analyst **140**, 2869 (2015).
Hou, D., Maheshwari, S., and Chang, H.-C., Biomicrofluidics **1**, 014106 (2007).
Hwang, H. and Park, J.-K., Lab Chip **9**, 199 (2009).
Jo, M. C. and Guldiken, R., Sens. Actuators A **196**, 1 (2013).
Jung, J. H., Destgeer, G., Ha, B. H., Park, J., and Sung, H. J., Lab Chip **16**, 3235 (2016).
King, L. V., Proc. R. Soc. London A **147**, 212 (1934).
Kinsler, L. E., Frey, A. R., Coppens, A. B., and Sanders, J. V., *Fundamentals of Acoustics* (John Wiley & Sons, 2000).
Kondoh, J., Shimizu, N., Matsui, Y., Sugimoto, M., and Shiokawa, S., Sens. Actuators A **149**, 292 (2009).
Laurell, T., Petersson, F., and Nilsson, A., Chem. Soc. Rev. **36**, 492 (2007).
Lewpiriyawong, N., Yang, C., and Lam, Y. C., Microfluid Nanofluid **12**, 723 (2012).
Li, H., Friend, J. R., and Yeo, L. Y., Biomed. Microdevices **9**, 647 (2007).
Lin, S.-C. S., Mao, X., and Huang, T. J., Lab Chip **12**, 2766 (2012).
Manor, O., Rezk, A. R., Friend, J. R., and Yeo, L. Y., Phys. Rev. E **91**, 053015 (2015).
Manor, O., Yeo, L. Y., and Friend, J. R., J. Fluid Mech. **707**, 482 (2012).

Martins, A. M. G., Glass, N. R., Harrison, S., Rezk, A. R., Porter, N. A., Carpenter, P. D., Plessis, J. D., Friend, J. R., and Yeo, L. Y., Anal. Chem. **86**, 10812 (2014).
Morse, P. M. and Ingard, K. U., *Theoretical Acoustics* (McGraw-Hill, 1986).
Nguyen, N.-T. and Wu, Z., J. Micromech. Microeng. **15**, R1 (2005).
Nyborg, W. L., *Acoustic Streaming*, edited by M. F. Hamilton and D. T. Blackstock (Academic Press, 1988), pp. 207–231.
Pamme, N., Eijkel, J. C., and Manz, A., J. Magn. Magn. Mater. **307**, 237 (2006).
Qi, A., Yeo, L. Y., and Friend, J. R., Phys. Fluids **20**, 074103 (2008).
Raghavan, R. V., Friend, J. R., and Yeo, L. Y., Microfluid. Nanofluid. **8**, 73 (2010).
Rajapaksa, A., Qi, A., Yeo, L. Y., Coppel, R., and Friend, J. R., Lab Chip **14**, 1858 (2014).
Rezk, A. R., Manor, O., Yeo, L. Y., and Friend, J. R., Proc. R. Soc. A **470**, 20130765 (2014).
Rogers, P. R., Friend, J. R., and Yeo, L. Y., Lab Chip **10**, 2979 (2010).
Rozenberg, L. D., *High-Intensity Ultrasonic Fields* (Plenum Press, 1971).
Schmid, L., Wixforth, A., Weitz, D. A., and Franke, T., Microfluid. Nanofluid. **12**, 229 (2012).
Schröder, C. T. and Scott, W. R., IEEE Trans. Geosci. Remote Sens. **38**, 1505 (2000).
Shi, J., Mao, X., Ahmed, D., Colletti, A., and Huang, T. J., Lab Chip **8**, 221 (2008).
Shi, J., Mao, X., Ahmed, D., Colletti, A., and Huang, T. J., Lab Chip **9**, 3354 (2009).
Shilton, R., Tan, M. K., Yeo, L. Y., and Friend, J. R., J. Appl. Phys. **104**, 014910 (2008).
Shilton, R. J., Mattoli, V., Travagliati, M., Agostini, M., Desii, A., Beltram, F., and Cecchini, M., Adv. Funct. Mater. **25**, 5895 (2015).
Shilton, R. J., Travagliati, M., Beltram, F., and Cecchini, M., Adv. Mater. **26**, 4941 (2014).
Shilton, R. J., Yeo, L. Y., and Friend, J. R., Sens. Actuators B **160**, 1565 (2011).
Stone, H. A., Stroock, A. D., and Ajdari, A., Annu. Rev. Fluid Mech. **36**, 381 (2004).
Tan, M. K., Friend, J. R., Matar, O. K., and Yeo, L. Y., Phys. Fluids **22**, 112112 (2010).
Tan, M. K., Friend, J. R., and Yeo, L. Y., Phys. Rev. Lett. **103**, 024501 (2009).
Tan, M. K., Yeo, L. Y., and Friend, J. R., EPL **87**, 47003 (2009).
Winkler, A., Harazim, S. M., Menzel, S. B., and Schmidt, H., Lab Chip **15**, 3793 (2015).
Yeo, L. Y., Chang, H.-C., Chan, P. P. Y., and Friend, J. R., Small **7**, 12 (2011).
Yeo, L. Y. and Friend, J. R., Annu. Rev. Fluid Mech. **46**, 379 (2014).
Yeo, L. Y., Friend, J. R., and Arifin, D. R., Appl. Phys. Lett. **89**, 103516 (2006a).
Yeo, L. Y., Hou, D., Maheshswari, S., and Chang, H.-C., Appl. Phys. Lett. **88**, 233512 (2006b).
Zeng, J., Chen, C., Vedantam, P., and Xuan, T.-R. T. X., Microfluid. Nanofluid. **15**, 49 (2013).